

Cation distribution and related properties of $\text{Mn}_x\text{Zn}_{1-x}\text{Fe}_2\text{O}_4$ spinel nanoparticles

Z. Klencsár^{1,*}, Gy. Tolnai², L. Korecz¹, I. Sajó², P. Németh²,
J. Osán³, S. Mészáros⁴, E. Kuzmann⁵

¹*Institute of Molecular Pharmacology, Research Centre for Natural Sciences, Hungarian Academy of Sciences, Pusztaszeri út 59-67, Budapest, 1025, Hungary*

²*Institute of Materials and Environmental Chemistry, Research Centre for Natural Sciences, Hungarian Academy of Sciences, Pusztaszeri út 59-67, Budapest, 1025, Hungary*

³*Centre for Energy Research, Hungarian Academy of Sciences, Konkoly-Thege út 29-33., Budapest, 1121, Hungary*

⁴*Institute of Nuclear Research of the Hungarian Academy of Sciences, Bem tér 18/c, Debrecen 4026, Hungary*

⁵*Institute of Chemistry, Loránd Eötvös University, Pázmány P. s. 1/A, Budapest, 1117, Hungary*

Abstract. $\text{Mn}_x\text{Zn}_{1-x}\text{Fe}_2\text{O}_4$ ($x = 0.05 \dots 0.9$) nanoparticles prepared via sol-gel hydrothermal process were investigated by X-ray powder diffractometry (XRPD), transmission electron microscopy (TEM), ^{57}Fe Mössbauer spectroscopy (MS), electron paramagnetic resonance spectroscopy (EPR), X-ray absorption near edge structure spectroscopy (XANES) and magnetic hysteresis measurements. XRPD measurements revealed a non-monotonic dependence of the cubic lattice parameter on the Mn concentration, which is interpreted as being the result of a corresponding variation in the inversion degree (concentration of Fe ions on the occupied tetrahedral lattice sites) of the studied spinels. XANES measurements indicated that the average oxidation state of Mn ions decreases with the applied Mn concentration, in contrast with Fe ions that were found to be exclusively in the 3+ oxidation state by MS measurements. EPR spectra recorded as a function of temperature enabled the determination of the characteristic anisotropy energy barrier of the superparamagnetic particles, and contributed to the clarification of peculiarities of the corresponding ^{57}Fe Mössbauer spectra. On the basis of the observed results the interdependences among the sample stoichiometry, the cubic cell parameter, the particle size, the inversion degree, the magnetic ordering temperature and the effective magnetic anisotropy are discussed.

Keywords: nanoparticles, spinel, ferrite, inversion

*Corresponding author. E-mail: klencsar.zoltan@ttk.mta.hu , Tel.: +36 1 438 1100 , Fax: +36 1 438 1143

1. INTRODUCTION

Magnetic nanoparticles are widely studied on account of their intriguing structural and magnetic properties (see, e.g., [1]) as well as of their potential applicability in various fields ranging from high-density data storage devices [2] to biomedical applications [3,4]. Nanoparticles of spinel ferrites are in particular interesting for both fundamental and applied science, because their magnetic properties such as coercivity, saturation magnetization and Curie temperature can be tuned to a great extent by the chemical substitution of elements in the tetrahedrally coordinated A and the octahedrally coordinated B sites of the rather flexible AB_2O_4 spinel structure [5,6,7,8]. While this kind of flexibility is certainly welcome from the applications' point of view, it is often a source of ambiguity concerning the connection between the atomic level structure and the associated magnetic properties of spinel nanoparticles. Namely, due to the readiness of the structure to incorporate the same kind of element in both the A and B sites and furthermore in different oxidation states, corresponding materials prepared according to the same stoichiometry may exist in a multitude of quasi-equilibrium states with substantial differences in their magnetic behavior. Consequently, apart from the knowledge of the stoichiometry, the proper assignment of magnetic properties to the underlying atomic-level structure requires also the establishment of the distribution and the oxidation state(s) of constituent elements situated in the A and B lattice sites [9]. The distribution in question can usually be sufficiently characterized by the degree of inversion (i), here defined as the fraction of filled A sites that are occupied by cations being originally attributed to the B sites on the basis of stoichiometry.

The importance of inversion in determining magnetic properties is clearly revealed by the case of the compound $ZnFe_2O_4$ that has a Néel temperature of ~ 9 K when prepared in bulk form as normal spinel ($i = 0$) via conventional high-temperature solid state synthesis, but displays magnetic ordering in the corresponding ^{57}Fe Mössbauer spectra already at $T = 40$ K and $T = 77$ K when prepared in the form of nanoparticles via sol-gel synthesis and high-energy ball milling, respectively [1]. The increased magnetic ordering temperature in the latter cases can be explained by the presence of a substantial amount of inversion ($i \approx 0.4$), and the consequently increased occurrence of strong antiferromagnetic Fe(T) - Fe(O) superexchange interactions, where Fe(T) and Fe(O) refer to iron at the tetrahedral A sites and

at the octahedral B sites, respectively. Recently, magnetization measurements showed that similar levels of inversion may lead to magnetic ordering in ZnFe_2O_4 nanoparticles already at temperatures 400–500 K [8], which indicates that the appearance of a paramagnetic signal in the ^{57}Fe Mössbauer spectra, as found in [1] at the above quoted lower temperatures, may be the result of superparamagnetism.

Apart from potentially giving rise to collective magnetic excitations and superparamagnetism, the nanometric size of magnetic particles may also be expected to influence the apparent magnetic properties due to the relatively high fraction of atoms in the surface layer of the particles, which may give rise, e.g., to an extended level of magnetic surface anisotropy [10]. In addition, correlation is sometimes found between the degree of inversion and the particle size (see, e.g., [11,12] for the case of MnFe_2O_4), suggesting that the degree of inversion in general tends to be higher in nanoparticles of smaller size. However, the presence and sign of such a correlation presumably also depends on the stoichiometry and the preparation method applied, as suggested by the recent results [13] where an opposite trend was observed for ZnFe_2O_4 nanoparticles.

In practice the uncertainty as regards the various structural attributes being capable to influence the apparent material properties of actual Mn-Zn ferrite samples makes it difficult to interpret the results of individual measurements in an unequivocal manner, which hinders the establishment of coherent knowledge concerning the connections among specifics of structure and properties of these compounds. Thus, the utilization of complementary experimental methods to characterize the same batch of samples seems to be inevitable for the further elucidation of these connections in Mn-Zn ferrites.

Accordingly, with the aim to gain further insight into the atomic level structure and related properties of Mn-Zn ferrites, we have carried out a study on $\text{Mn}_x\text{Zn}_{1-x}\text{Fe}_2\text{O}_4$ ($x = 0.05, 0.1, 0.25, 0.5, 0.7, 0.75, 0.8, 0.9$) nanoparticle powders by several complementary experimental methods such as X-ray powder diffractometry (XRPD), transmission electron microscopy (TEM), ^{57}Fe Mössbauer spectroscopy (MS), electron paramagnetic resonance spectroscopy (EPR), X-ray absorption near edge structure spectroscopy (XANES) and magnetic hysteresis measurements.

2. EXPERIMENTAL

$\text{Mn}_x\text{Zn}_{1-x}\text{Fe}_2\text{O}_4$ ($x = 0.05, 0.1, 0.25, 0.5, 0.7, 0.75, 0.8, 0.9$) nanopowders were prepared via sol-gel hydrothermal process starting from a mixed solution of Mn^{2+} , Zn^{2+} and Fe^{3+} salts in strongly alkaline aqueous medium. $\text{MnCl}_2 \times 4 \text{H}_2\text{O}$, ZnCl_2 and $\text{FeCl}_3 \times 6 \text{H}_2\text{O}$ were used as metal ion sources and NaOH for pH adjustment in starting solutions. The chemicals were reagent grade and purchased from Reanal, Hungary. The Fe^{3+} concentration was fixed at 40 mM in all the synthesis processes, whereas the amounts of Mn and Zn salts were determined by considering the actual Mn^{2+} and Zn^{2+} stoichiometry. In a typical procedure, the calculated amounts of salts were dissolved in double distilled water at room temperature and the pH was adjusted to 11 using 0.1 M freshly prepared NaOH solution. The volume of the final solution in the reaction vessel was 500 ml. In the next step the reaction mixture was homogenized for half an hour at room temperature under vigorous stirring. The formation of ferrite nanoparticles takes place by the conversion of metal salts into mixed amorphous hydroxide precipitates, which occurs immediately after the addition of NaOH. Transformation of hydroxides into ferrites requires a higher temperature, minimum 90°C, and several hours of reaction time. In our case boiling conditions were applied for 4 hours in order to complete the hydroxide to spinel ferrite transformation and to promote the formation of well-crystallized particles. After the reaction was completed, the ferrite particles were separated by centrifugation, purified by washing several times with distilled water, and then dried at 60°C.

Transmission electron microscopy (TEM) measurements of the samples were carried out by a Morgagni 268D (100 kV) transmission electron microscope.

X-ray powder diffraction (XRPD) patterns were obtained at room temperature by a Philips PW3710 based PW1050 Bragg-Brentano parafocusing goniometer by using Cu K_α radiation ($\lambda \approx 0.154186 \text{ nm}$), graphite monochromator and proportional counter.

^{57}Fe Mössbauer spectra of the powders were recorded in transmission geometry by using $^{57}\text{Co}(\text{Rh})$ radioactive source and conventional spectrometers (Wissel and KFKI) operated in constant acceleration mode. ^{57}Fe isomer shift values are given relative to that of α -iron at room temperature.

EPR measurements were carried out on a Bruker ElexSys E500 X-band spectrometer on powders being either embedded in paraffin wax or mixed with MgO powder. Unless

otherwise noted, the conditions of EPR measurements involved a single scan with modulation frequency of 100 kHz, modulation amplitude of 0.1 G and microwave power lying below 20.6 mW. Samples in paraffin wax were magnetically oriented by cooling them from above the melting point of wax ($T_m \approx 320$ K) to ~ 300 K in 1.4 T external magnetic field. Variable temperature measurements below T_m were performed first during cooling of the sample down to 140 K where the sample was rotated by 90° , and then during heating of the sample to just above T_m . As MgO-mixed samples did not show appreciable dependence on sample orientation, only the data recorded during the cooling of the samples are presented.

X-ray diffractograms, Mössbauer and EPR spectra were analyzed by using the MossWinn program [14] that was complemented with auxiliary libraries providing the fitting functions for XRPD and EPR measurements.

XANES measurements were performed on the samples with $x = 0.1, 0.25, 0.5, 0.75$ and 0.9 , at the micro-fluorescence beamline L of the DORIS III storage ring operated by HASYLAB at the German Electron Synchrotron DESY (Hamburg, Germany). For comparison purposes, XANES spectra were recorded from powdered standards of known Mn oxidation state prepared from pro analysis grade chemicals of MnO_2 (Mn^{4+}), MnOOH (Mn^{3+}) and MnCO_3 (Mn^{2+}). Background removal and normalization of the XANES spectra was performed by using the ATHENA software package [15].

Magnetic hysteresis measurements were carried out at room temperature on powdered samples using a custom made AC magnetometer. Driving field frequencies of 133 Hz and 400 kHz were applied, with the driving field amplitude being in the range of 6.5...121 mT for 133 Hz and 6.5 mT for 400 kHz.

3. RESULTS AND DISCUSSION

TEM images (Figure 1) display nanosized $\text{Mn}_x\text{Zn}_{1-x}\text{Fe}_2\text{O}_4$ particles with a wide size-distribution ranging from ~ 2 -3 nm (as clearly shown for $x = 0.7$ and 0.9) up to ~ 50 nm (as shown for $x = 0.8$). With the exception of the sample with $x = 0.8$, the presence of particles with a size above 25 nm is not typical in the samples. The shape of the particles is generally well approximated by a sphere, with the exception of the large rhomboid particles of the sample with $x = 0.8$ (Figure 1).

In agreement with the nanosized nature of the particles, X-ray diffractograms of the samples display broad diffraction peaks that can be well indexed in accordance with the cubic spinel crystal structure (Figure 2). Apart from the relatively sharp peaks associated with residual NaCl crystals (being a byproduct of the preparation procedure) or Si (added to the samples to facilitate calibration of the axis of diffraction angles even in the absence of NaCl) the diffractograms do not refer to secondary phases. The peaks belonging to the spinel phase were fitted to Lorentzians whose position and width were determined on the basis of Bragg's law and Scherrer's equation, respectively (see [16]). The cubic lattice parameters and the crystallite sizes thus derived are summarized in Table 1. The lattice parameter (a) of our $\text{Mn}_x\text{Zn}_{1-x}\text{Fe}_2\text{O}_4$ samples display a Mn-concentration dependence that is different from that (see [17]) characteristic to analogous bulk samples prepared via high-temperature synthesis. In the latter case a shows a near linear increase with Mn concentration [17] in accordance with the higher ionic radius of high-spin Mn^{2+} (0.0655 nm [18]) with respect to that of Zn^{2+} (0.058 nm [18]). The lattice parameter of oxide spinels increases monotonously (and near linearly) with the average cation radius of the constituting cations [19]. The peculiar x dependence of a in our samples must thus be connected to the presence of A-site high-spin Fe^{3+} that on account of its small ionic size (0.0485 nm [18]) can lead to a decrease in the average cation radius. This can explain the lack of increase in a despite the presence of Mn in the system. Namely, by considering the ionic radii (see [18,20,21] and Figure S1 in the supplement) of Zn^{2+} , high-spin Fe^{3+} , and high-spin Mn^{2+} and Mn^{3+} , there appears to be no other way to achieve a reduction of the average cation radius by cation substitution or site exchange between the cations. In the present spinel system the stoichiometric amount of iron at the tetrahedral A site equals to the spinel's inversion degree i . The corresponding amount of octahedral B sites may be filled either by Zn or Mn. As the ionic radius of high-spin $\text{Mn}^{3+}(\text{O})$ and $\text{Fe}^{3+}(\text{O})$ can be taken to be equal [18,20,21], Mn^{3+} can be expected to compete successfully for the vacant octahedral sites. Mn^{3+} may also be the preferred cation for octahedral sites on account of its $3d^4$ electronic state and the associated crystal-field stabilization energy [19,22]. Therefore, we hypothesize that Mn fills (in the form of high-spin Mn^{3+}) all octahedral sites left vacant by iron taking tetrahedral sites, and Zn is restricted exclusively to the tetrahedral site. Thus, the composition of the samples may be written as

$(\text{Zn}_{1-x}^{2+}\text{Mn}_{x-i}^{2+}\text{Fe}_i^{3+})[\text{Fe}_{2-i}^{3+}\text{Mn}_i^{3+}]\text{O}_{4+d}$, where square brackets represent the cations situated at the octahedral sites. The extra positive electric charge of $Q = ie$ appearing per formula unit may then be compensated by excess oxygen (d) at the surface of the nanoparticles [23].

Assuming that the observed variation of the cubic lattice parameter (Table 1) can be ascribed exclusively to the variation of x and i , we may calculate i as a function of a and x as follows. The bond lengths d_{AO} and d_{BO} between oxygen and the cations at tetrahedral A and octahedral B sites, respectively, can be written as [19]:

$$\begin{aligned} d_{\text{AO}} &= a\sqrt{3}(u-1/4) \\ d_{\text{BO}} &= a\sqrt{2(u-3/8)^2 + (5/8-u)^2} \end{aligned} \quad (1)$$

where u denotes the oxygen anion displacement parameter. By eliminating u from the above equations we can express the lattice parameter as a function of d_{AO} and d_{BO} :

$$a = \frac{8}{11\sqrt{3}} (5d_{\text{AO}} + \sqrt{33d_{\text{BO}}^2 - 8d_{\text{AO}}^2}). \quad (2)$$

The average bond lengths can be estimated as the sum of the average cation radii and the oxygen ion radius R :

$$\begin{aligned} d_{\text{AO}} &= R + \langle r_{\text{A}} \rangle = R + (1-x)r_{\text{A}(\text{Zn}^{2+})} + (x-i)r_{\text{A}(\text{Mn}^{2+})} + ir_{\text{A}(\text{Fe}^{3+})} \\ d_{\text{BO}} &= R + \langle r_{\text{B}} \rangle = R + (1-i/2)r_{\text{B}(\text{Fe}^{3+})} + (i/2)r_{\text{B}(\text{Mn}^{3+})} \end{aligned} \quad (3)$$

where $r_{\text{A}(\text{X}^{n+})}$ and $r_{\text{B}(\text{X}^{n+})}$ denote the ionic radius of a cation X^{n+} at the lattice position A and B, respectively. For the ionic radii of cations we use the following numerical values [18,20,21]: $r_{\text{A}(\text{Zn}^{2+})} = 0.058 \text{ nm}$, $r_{\text{A}(\text{Mn}^{2+})} = 0.0655 \text{ nm}$, $r_{\text{A}(\text{Fe}^{3+})} = 0.0485 \text{ nm}$,

$r_{\text{B}(\text{Fe}^{3+})} = 0.0645 \text{ nm}$ and $r_{\text{B}(\text{Mn}^{3+})} = 0.0645 \text{ nm}$. Substituting the above expressions into Eq. (2) and making use of $r_{\text{B}(\text{Fe}^{3+})} = r_{\text{B}(\text{Mn}^{3+})}$ we can describe a in the function of x , i and the ionic radii.

For $x = i = 0$ we obtain

$$a(R) = \frac{8}{11\sqrt{3}} (5(R + r_{\text{A}(\text{Zn}^{2+})}) + \sqrt{33(R + r_{\text{B}(\text{Fe}^{3+})})^2 - 8(R + r_{\text{A}(\text{Zn}^{2+})})^2}), \quad (4)$$

which equation can be used to calculate R appropriate for the present compounds on the basis of the cubic lattice parameter of the normal spinel ZnFe_2O_4 . For the latter we accept the value of $a = 0.8442(5) \text{ nm}$ reported in [24], from which, by the use of Eq. (4), we observe

$R \approx 0.13878(10)$ nm as the radius of oxygen ions, in good agreement with that (0.138 nm) reported in [18,20,21]. Substituting the above quoted ionic radii and $R = 0.13878$ nm in Eq. (3), and solving the corresponding Eq. (2) for i we obtain

$$i(a, x) = \frac{2\sqrt{6}\sqrt{38740086 - (6250a/\text{nm})^2} + 1125x - (31250\sqrt{3})a/\text{nm} + 29517}{2550}, \quad (5)$$

where a/nm denotes the numerical value of a in nm. By substituting the corresponding values of x and a (Table 1) into Eq. (5) we observe the degree of inversion as a function of x as listed in Table 1. For $x = 0.05$ and $x = 0.1$ we observe $i = 0.05$ (i.e. Mn occupies exclusively octahedral B sites in the form of Mn^{3+}) and $i = 0$ (i.e. Mn is present only on the tetrahedral A sites in the form of Mn^{2+}) inside the experimental error, respectively. Except for $x = 0.1$, inversion increases with Mn concentration up to $x = 0.75$ with a maximal value of $i \approx 0.454(5)$. For $x > 0.75$ the inversion decreases, reaching a value of $i \approx 0.35(3)$ for $x = 0.9$. The calculated inversion values are larger than those found for bulk $\text{Mn}_x\text{Zn}_{1-x}\text{Fe}_2\text{O}_4$ ferrites [17], but they nevertheless fall within the range usually obtained for manganese ferrites [11,22,25,26]. The obtained range of anion parameter values $u = 0.383\dots 0.385$ (see Table 1), calculated on the basis of Eq. (1), also corroborates the presence of inversion in our samples (see [19,27]).

The average crystallite size (Table 1) remains below 10 nm for all the studied $\text{Mn}_x\text{Zn}_{1-x}\text{Fe}_2\text{O}_4$ samples, and it shows a maximum as a function of x for $x = 0.5$. For $x > 0.5$ the trend characterizing our samples is the opposite of that reported in [5,25,28] where the particle size was found to increase with Mn concentration.

At room temperature ^{57}Fe Mössbauer spectra of the studied samples display (see Figure S6 in supplement) a quadrupole doublet and—in the case of $x = 0.7, 0.75$ and 0.8 —a magnetic sextet with an isomer shift value lying (for both) in the range of $0.33\dots 0.38$ mm/s. The found range of isomer shift values is typical for high-spin Fe^{3+} and excludes the presence of Fe^{2+} in our samples. It also agrees well with isomer shift values reported earlier for Mn-Zn ferrite nanoparticles [6,29,30]. The simultaneous presence of a magnetic sextet and a doublet component in the ^{57}Fe Mössbauer spectra is typical for superparamagnetic nanopowders with a particle size distribution. It must be a higher characteristic anisotropy energy barrier (KV , where V is the volume and K is the magnetic anisotropy energy density) of the nanoparticles

in the samples with $x = 0.7, 0.75$ and 0.8 that results in a sextet component in their room-temperature Mössbauer spectra in contrast with the rest of the samples. Indeed, X-ray diffractograms (Figure 2) suggest a wider distribution in the size of the crystallites for $x > 0.5$. This may be connected to the presence of particles with a higher volume and a correspondingly increased anisotropy energy barrier in the samples with $x = 0.7, 0.75$ and 0.8 (Table 1). At the same time, an increase in K can also be expected due to the presence of B-site Mn^{3+} ions that on account of their $3d^4$ electronic state and associated Jahn-Teller activity can display a single-ion magnetocrystalline anisotropy that is large compared to what can be expected from other metal ions (having either filled or half-filled valence shells) in the system [31]. As a result, K should increase with the degree of inversion that in our model also gives the stoichiometric amount of Mn^{3+} on the octahedral B sites. It is then revealing to see that the samples with $x = 0.7, 0.75$ and 0.8 , in which case a magnetic sextet is observed in the room-temperature Mössbauer spectra, are at the same time those for which the highest degree of inversion was predicted by our model (Table 1).

In the low-temperature ^{57}Fe Mössbauer spectra of the $\text{Mn}_x\text{Zn}_{1-x}\text{Fe}_2\text{O}_4$ samples (Figure 3), the spectral shape changes with x in a non-monotonous manner, i.e. apart from x the system must have further degrees of freedom available for the alteration of its magnetic state as seen by Mössbauer spectroscopy. One of these is the particle size distribution, regarding which the spectra reveal in a rather obvious way that the samples with $x > 0.5$ are subject to a wide particle size distribution whereas those with $x \leq 0.5$ consist of particles with a more uniform size.

Due to collective magnetic excitations the hyperfine magnetic field reflected by the sextet component may be smaller than that characteristic to the bulk material. Therefore, the temperature dependence of the largest hyperfine magnetic field displayed by the ^{57}Fe Mössbauer spectra allows us to estimate only a *lower* limit of the Curie temperature of the samples with $x = 0.5, 0.7, 0.75$ and 0.8 . For a given sample the temperature-dependence of the largest characteristic hyperfine magnetic field, obtained on the basis of the corresponding hyperfine magnetic field distributions, was fitted to a Brillouin curve with $J = 5/2$. The Curie temperature estimates obtained in this way are shown in Figure 6.

Figure 4 displays EPR spectra measured with the sample orientation being either parallel or perpendicular to the—horizontal—static magnetic field of the spectrometer. The resonance curve is shifted towards higher magnetic fields when the samples are rotated into the state of perpendicular orientation. The magnitude of resonance-field shift is proportional to the effective anisotropy field of the particles. Comparison of Figure 4 with Figure 3 reveals a remarkable correlation between low-temperature Mössbauer spectra and the room-temperature EPR measurements: for samples that show the lowest effective magnetic anisotropy field at $T \approx 300$ K ($x = 0.1, 0.25, 0.8, 0.9$) the low-temperature Mössbauer spectra display a dominant superparamagnetic doublet component, for those that show higher but still only moderate anisotropy field ($x = 0.05, 0.7$) we observe either a spectral shape transitional between a full-blown sextet and a superparamagnetic doublet ($x = 0.05$) or one to which the sextet and the superparamagnetic doublet component contributes with comparable area ($x = 0.7$), and finally for samples with the largest magnetic anisotropy field ($x = 0.5, 0.75$) we observe a Mössbauer spectrum that is dominated by a majority sextet component. This correlation indicates that the non-monotonous development of the spectral shape of low-temperature Mössbauer spectra (Figure 3) as a function of the x Mn concentration is indeed caused by a corresponding non-monotonous x dependence of the magnitude of the particles' anisotropy energy barrier.

Inhomogeneous EPR-peak broadening is expected to display a Gaussian shape and a decay with increasing temperature that ends when the Curie temperature is reached. The temperature dependence of the Gaussian broadening (i.e. Gaussian FWHM width, Γ_G) is depicted in Figure 5 for all the studied samples. The temperature at which Γ_G tends to drop to zero can be interpreted as an estimation of the Curie temperature. The T_c values thus obtained are drawn in Figure 6 together with the corresponding values (T_c^{MS}) obtained on the basis of Mössbauer measurements, and with the functional dependence of $T_c(x)$ predicted for normal $\text{Mn}_x\text{Zn}_{1-x}\text{Fe}_2\text{O}_4$ spinels [32]. The obtained T_c values are either higher than or equal—inside the experimental error—to those expected for normal $\text{Mn}_x\text{Zn}_{1-x}\text{Fe}_2\text{O}_4$ compounds. Higher T_c values can be attributed to the strong antiferromagnetic superexchange interaction between Fe^{3+} ions situated on neighboring tetrahedral and octahedral sites. The T_c^{MS} values determined on the basis of Mössbauer measurements are all smaller than their EPR-derived counterparts,

which supports the view that the particles contributing to the well-developed sextet components in the ^{57}Fe Mössbauer spectra are subject to collective magnetic excitations. A possible exception is the sample with $x = 0.75$, in which case T_c^{MS} agrees with the Curie temperature of the corresponding normal spinel (Figure 6). Namely, this remarkable agreement suggests that the largest particles of this sample behave like a normal spinel, whereas smaller ones (that contribute to the superparamagnetic doublet component) show a higher T_c (as revealed by the EPR measurements) possibly due to an enhanced degree of inversion and associated strong $\text{Fe}^{3+}(\text{T}) - \text{Fe}^{3+}(\text{O})$ superexchange interaction. Similarly high (700 – 800 K) T_c values were already observed for analogous but larger (13 – 30 nm) nanoparticles with $x = 0.6$ [25]. A possible influence of superparamagnetism on these T_c values is made unlikely by the observation that the T_c values of the samples with $x = 0.5, 0.7, 0.8$ and 0.9 increase with x despite the decreasing trend found in their average crystallite size (Table 1).

Figure 7 shows the temperature dependence of the superparamagnetic peak's central resonance field (B_{SP}) characterizing the EPR spectra of wax-embedded oriented and MgO-embedded random powders for the typical cases of $x = 0.05$ and $x = 0.5$. The temperature dependence of B_{SP} can be interpreted as to be caused by the temperature dependence of the effective anisotropy field. In all the cases the magnetic orientation of the samples is made evident by an increase in B_{SP} when the sample is rotated by 90° at $T = 140$ K. By comparing the measurements carried out on the oriented and on random (MgO-mixed) powder samples, two distinctive features can be observed: for the samples with $x = 0.05, 0.1$ and 0.7 the B_{SP} resonance field (and thus the effective magnetic anisotropy field) observed in the perpendicular orientation coincides (to a good approximation) with that observed for the random sample, whereas for $x = 0.25, 0.5, 0.75, 0.8$ and 0.9 the B_{SP} resonance field of the random powder lies between that characteristic to parallel and perpendicular orientations. In the former case the presence of a uniaxial magnetic anisotropy axis fixed to the corresponding samples' particles is excluded, because in the presence of such uniaxial magnetic anisotropy the detected effective magnetic anisotropy field could not be the same in the perpendicularly oriented and in the random powders. In contrast, the intermediate (i.e. between the \parallel and \circ series on Figure 7) nature of B_{SP} in the random powders of the remaining compositions are in

qualitative agreement with the expectations for a uniaxial magnetic anisotropy axis fixed to the particle frame. The temperature dependent magnitude of the overall effective anisotropy field may be approximated by the difference between the actual B_{SP} resonance field and the resonance field measured in the paramagnetic state of the material. As for some of the samples the latter state could not be reached in the applied temperature interval (Figure 5), we approximate the resonance field characteristic to the paramagnetic state (B_p) with the common value of $B_r(g_e) \approx 3365$ G corresponding to the electron g factor (g_e) at the measuring frequency of $f = 9.43$ GHz.

The anisotropy field of the present samples can be seen as the sum of two contributions: one that depends on the orientation of the magnetically oriented samples, and one that does not depend on the sample orientation and is therefore the same for the oriented and the random (MgO-mixed) samples. It is mainly the latter that makes B_{SP} decrease with decreasing temperature even for the random and the perpendicularly oriented samples (Figure 7). (A similar effect was observed for $Mn_{0.5}Zn_{0.5}Fe_2O_4$ nanoparticles at ~ 40 K [33].) The anisotropy contribution that depends on sample orientation is likely to be originating from magnetocrystalline anisotropy [31]. On the other hand, the contribution influencing the mean resonance field also of the MgO-mixed random samples can be an induced type of (uniaxial) anisotropy that is connected to the orientation of the magnetic moments of the individual particles by the sweeping field of the spectrometer during the measurement (the direction of the orienting field becoming the easy axis of magnetization). For particles whose magnetic moment undergoes thermal fluctuations, both mentioned parts of the magnetic anisotropy field will be subject to averaging [34,35]. It is our hypothesis that the temperature dependence of this averaging effect can be seen as the main source of the temperature dependence of $B_{SP,\parallel}$ at around 140 K.

According to [34] at low enough temperatures when $mB/(k_B T) \gg 1$, where m is the magnetic moment of the particles and B is the flux density of the applied magnetic field, in the case of a particle with uniaxial magnetic anisotropy the magnetic anisotropy field averaged due to thermal fluctuations ($B_{a,eff}$) approaches the corresponding bulk value (B_a) with decreasing temperature approximately linearly as

$$\frac{B_{a,\text{eff}}}{B_a} = 1 - \frac{2k_B T}{mB} \quad (6)$$

As one can indeed approximate $B_{\text{SP},\parallel}$ with a linear function at around 140 K (Figure 7), we have used the corresponding slope values (Table 2) to calculate the particles' characteristic magnetic anisotropy energy barrier in temperature units ($E_a/k_B = KV/k_B$) on the basis of the above formula, by taking into account that $B_a = 2K/M$ (see [36,37]) where M denotes the magnetization of the particles. The results obtained in this way (Table 2, Figure S7) display excellent correlation with low-temperature Mössbauer measurements (Figure 3), as revealed by the following observations.

- (1) Compositions ($x = 0.1$ and 0.25) for which the sextet component is the least developed in the range of 83-94K turn out to have an anisotropy energy barrier whose value is among the smallest observed and lies well below the temperature range of Mössbauer measurements. Furthermore, the slightly more developed magnetic relaxation pattern of the sample with $x = 0.25$ is also appropriately reflected in the higher anisotropy energy barrier.
- (2) Compositions that in the Mössbauer spectra display either a transitional spectral shape ($x = 0.05$) or a comparable contribution from a sextet and a doublet component ($x = 0.7$) turn out to have an E_a/k_B value that lies close and slightly above the range of measuring temperatures.
- (3) Compositions ($x = 0.8$ and 0.9) where a contribution from a sextet component though observed remains below 50% at 83 K display an E_a/k_B value below 83 K. Furthermore, the larger fraction of sextet component in the Mössbauer spectrum (Figure 3) of the sample with $x = 0.9$ is accompanied with an anisotropy energy value larger than that characterizing the sample with $x = 0.8$.
- (4) Compositions ($x = 0.5$ and 0.75) where a sextet component dominates the Mössbauer spectrum at $T \approx 92 - 94$ K display an E_a/k_B value well above 94 K.
- (5) The $E_a/k_B = 152(9)$ K obtained for $\text{Mn}_{0.5}\text{Zn}_{0.5}\text{Fe}_2\text{O}_4$ is in agreement with the temperature range in which the corresponding Mössbauer spectra (Figure S8 in supplement) undergo a transition from a superparamagnetic doublet to a magnetic sextet.
- (6) In comparison with the sample of $x = 0.75$, the lower anisotropy energy barrier of the particles in the sample with $x = 0.7$ explains why its Mössbauer spectrum displays a lower

contribution from a sextet component at 83 K than the Mössbauer spectrum of the sample with $x = 0.75$ at 92 K, despite the smaller average crystallite size of the latter (Table 1).

On the basis of the observed E_a values we may estimate the characteristic volumetric anisotropy energy density ($K = E_a/V$) of the samples by assuming that the shape of the particles is well approximated by a sphere whose diameter is given by the average crystallite size (Table 1). The magnitude of the K values (Table 2) span a reasonable range: whereas bulk MnFe_2O_4 was reported to have an anisotropy density of $0.25 \times 10^4 \text{ J/m}^3$ at room temperature, the low temperature (5K) limit of K for similarly sized nanoparticles of MnFe_2O_4 was found to be $8.5 \times 10^4 \text{ J/m}^3$ [38]. In the range of $x = 0.1 \dots 0.7$ the magnetic anisotropy energy density increases with the calculated inversion degree (Table 1) in accordance with the prediction of our model making Mn^{3+} at octahedral sites responsible for the increase of magnetocrystalline anisotropy. The enhanced anisotropy energy density of the samples with the smallest average particle size ($x = 0.05, 0.75, 0.8, 0.9$) may be attributed to a contribution of magnetic surface anisotropy that increases with the particles' surface-to-volume ratio.

As in our model inversion directly gives the stoichiometric amount of Mn^{3+} in the system, it should also be reflected in the average oxidation state of Mn ions. To verify this interdependence we have performed Mn K-edge XANES measurements on the samples with $x = 0.1, 0.25, 0.5, 0.75$ and 0.9 . The average Mn oxidation state is reflected in the chemical shift of the absorption edge with respect to that of the known standards of MnCO_3 , MnOOH and MnO_2 . In contrast with [39], we clearly observe a chemical shift in the Mn K-edge as a function of the x Mn concentration, as shown in Figure 8: obviously, the K-edge shifts to lower energies and consequently the average oxidation state of Mn decreases with increasing x . This tendency provides a clear proof for Mn being present in different oxidation states in our samples, with the higher oxidation states prevailing in samples with lower Mn concentration. At the same time, the actual average oxidation states reflected by the XANES measurements are puzzling because they indicate the presence of Mn^{4+} in our samples, first of all for the compositions with $x = 0.1$ and 0.25 in which case the K-edge is situated between that of MnOOH and MnO_2 (Figure 8). Nevertheless, Mn^{4+} has already been found by the means of XANES in analogous nanoparticles of $\text{Mn}_{0.5}\text{Zn}_{0.5}\text{Fe}_2\text{O}_4$ [23], where it was attributed to a stoichiometric excess of oxygen accumulating on the surface of nanoparticles and the

corresponding oxidation of Mn in the surface atomic layers. Accepting this to be the case in our samples as well, the contradiction between the exclusively Mn^{2+} state we evaluated for $\text{Mn}_{0.1}\text{Zn}_{0.9}\text{Fe}_2\text{O}_4$ on the basis of the lattice parameters (Table 1) and the high(est) (roughly $\text{Mn}^{3.5+}$) average oxidation state reflected by the energy of the corresponding Mn K-edge (Figure 8) may be resolved by considering that in order to compensate for the excess negative charge of surface oxygen more Mn^{4+} needs to be formed in the surface layer when the core of the particles is normal spinel with Mn^{2+} only, than in the case when the core is partially inverse spinel with i stoichiometric amounts of Mn^{3+} . When the core is characterized by a higher degree of inversion, and a consequently higher amount of Mn^{3+} , then the excess negative charge of surface oxygen may be fully compensated already by the formation of Mn^{3+} in the core, and thus there is no need for the formation of Mn^{4+} in the surface layer. This may also be the reason why for the samples with higher degree of inversion ($x = 0.75$ and 0.9) the average Mn oxidation states reflected by the Mn K-edge fall, as expected, between $2+$ and $3+$, and are actually in quite good agreement with the average Mn oxidation states (2.4 for $x = 0.9$ and 2.6 for $x = 0.75$) calculated on the basis of the predicted degree of inversion (Table 1) in these samples.

From the point of view of the preparation process the differences observed among the samples concerning the occurrence of manganese in different oxidation states may be rooted in the variation of the starting reaction solution's $[\text{OH}^-/\text{Mn}^{2+}]$ molar ratio with the stoichiometry. Namely, lower manganese concentration is accompanied by a higher $[\text{OH}^-/\text{Mn}^{2+}]$ ratio, which promotes the transformation of Mn^{2+} to Mn^{3+} , and the following disproportionation reaction of Mn^{3+} to Mn^{2+} and Mn^{4+} [40].

Specific hysteresis energy loss of $\text{Mn}_x\text{Zn}_{1-x}\text{Fe}_2\text{O}_4$ nanoparticles (being of relevance for the possible biomedical application of Mn-Zn ferrite nanoparticles as heat mediators in magnetic hyperthermia treatments [4]) were calculated on the basis of magnetic hysteresis curves. The room-temperature hysteresis loss measured with a driving AC field amplitude of 6.5 mT, at 133 Hz as well as at 400 kHz driving field frequency, takes on its maximum value for $x = x_{\text{max}} = 0.75$, for which composition we have observed the largest degree of inversion (Table 1) and largest T_c (Figure 6) among the samples. With the deviation of x from x_{max} the hysteresis loss was found to decrease steeply. For the applied range of driving magnetic field

amplitudes the coercive field of the samples remains below $\sim_0H_c = 6$ mT for all x with the exception of $x = 0.8$ where the larger particles, detected also via the TEM images (Figure 1), led to considerably larger \sim_0H_c when the hysteresis curve was recorded with the driving field amplitude set to ~ 55 mT (Figure S9 in supplement) and ~ 121 mT.

4. CONCLUSIONS

$Mn_xZn_{1-x}Fe_2O_4$ nanoparticles prepared via sol-gel hydrothermal process with x ranging from 0.05 to 0.9 have been found to display variable morphological, structural and magnetic properties. The hypothesis relating the observed cubic lattice parameter to the composition and to the distribution of magnetic metal ions among the octahedral and tetrahedral sites enabled the estimation of the studied spinel ferrites' inversion degree that was considered together with the composition and the particle size to account for the non-monotonic Mn concentration dependence of features displayed by the observed ^{57}Fe Mössbauer- and X-band EPR spectra. A coherent interpretation of the main aspects of the Mössbauer and EPR results could be given on the basis of the superparamagnetic nature of the nanoparticles, and enabled the calculation of reasonable estimates for magnetic material properties such as the Curie temperature, the anisotropy energy barrier and the effective volumetric anisotropy energy density.

The presence of Mn in different valence states was confirmed by Mn K-edge XANES measurements; the relatively large single-ion magnetocrystalline anisotropy of Mn^{3+} , occurring at octahedral sites due to inversion, was made responsible for the influential effect of inversion on the magnitude of magnetic anisotropy, and the presence of Mn^{4+} suggested by XANES was attributed to Mn ions at or near the particle surface where they could serve for the compensation of the extra negative charge of surface oxygen ions.

Specific hysteresis energy loss measurements as a function of x demonstrated the variation of the fitness of $Mn_xZn_{1-x}Fe_2O_4$ nanoparticles for being utilized in hyperthermia treatment applications.

Overall the present work demonstrates that material properties of $Mn_xZn_{1-x}Fe_2O_4$ spinel ferrite nanoparticles such as composition, inversion, particle size and the distribution thereof can have significant influence on the apparent relevant magnetic properties such as the Curie

temperature, magnetic anisotropy and superparamagnetism, and consequently the unambiguous elucidation of the interdependences between specific magnetic, structural or morphological material properties requires the simultaneous assessment of the inversion degree and the remaining, more directly accessible relevant properties of the samples by the application of suitably chosen complementary experimental methods. In particular, on the basis of our results, it appears that in the case of the present class of compounds powder X-ray diffractometry can directly provide a reasonable estimation of the degree of inversion via the cubic lattice parameter, whereas by considering the superparamagnetic nature of the nanoparticles ^{57}Fe Mössbauer spectroscopy and EPR spectroscopy can yield useful information concerning the attributes of the particles' magnetic anisotropy.

Acknowledgements

The present work was in part supported by GVOP-3.2.1.-2004-04-0214/3.0. The XANES measurements were carried out at the light source DORIS III at DESY, a member of the Helmholtz Association (HGF). We would like to thank Karen Appel for assistance in using beamline L. Micro-XANES studies have received funding from the European Community's Seventh Framework Programme (FP7/2007-2013) under grant agreement no. 226716.

References

- [1] F.S. Li, L. Wang, J.B. Wang, Q.G. Zhou, X.Z. Zhou, H.P. Kunkel, G. Williams: *J. Magn. Magn. Mater.* **268** (2004) 332.
- [2] X.W. Wu, H. Zhou, R.J. M. van de Veerdonk, T.J. Klemmer, C. Liu, N. Shukla, D. Weller, M. Tanase, D.E. Laughlin: *J. Appl. Phys.* **93** (2003) 7181.
- [3] A. Figuerola, R. Di Corato, L. Manna, T. Pellegrino: *Pharmacological Research* **62** (2010) 126.
- [4] S. Laurent, S. Dutz, U.O. Häfeli, M. Mahmoudi: *Adv. Colloid Interface Sci.* **166** (2011) 8.
- [5] R. Arulmurugan, B. Jeyadevan, G. Vaidyanathan, S. Sendhilnathan: *J. Magn. Magn. Mater.* **288** (2005) 470.
- [6] R. Arulmurugan, G. Vaidyanathan, S. Sendhilnathan, B. Jeyadevan: *J. Magn. Magn. Mater.* **298** (2006) 83.

- [7] G. Vaidyanathan, S. Sendhilnathan, R. Arulmurugan: *J. Magn. Magn. Mater.* **313** (2007) 293.
- [8] S.J. Stewart, I.A. Al-Omari, F.R. Sives, H.M. Widatallah: *J. Alloys Compd.* **495** (2010) 506.
- [9] Z.J. Zhang, Z.L. Wang, B.C. Chakoumakos, J.S. Yin: *J. Am. Chem. Soc.* **120** (1998) 1800.
- [10] F. Gazeau, J.C. Bacri, F. Gendron, R. Perzynski, Yu.L. Raikher, V.I. Stepanov, E. Dubois: *J. Magn. Magn. Mater.* **186** (1998) 175.
- [11] M.H. Mahmoud, H.H. Hamdeh, A.I. Abdel-Mageed, A.M. Abdallah, M.K. Fayek: *Physica B* **291** (2000) 49.
- [12] A.H. Morrish, Z.W. Li, X.Z. Zhou: *J. Phys. IV* **7 C1** (1997) 513.
- [13] S.J. Stewart, S.J.A. Figueroa, M.B. Sturla, R.B. Scorzelli, F. García, F.G. Requejo: *Physica B* **389** (2007) 155.
- [14] Z. Klencsár, E. Kuzmann, A. Vértes: *J. Radioanal. Nucl. Chem.* **210** (1996) 105.
- [15] B. Ravel, M. Newville: *J. Synchrotron Rad.* **12** (2005) 537.
- [16] A.W. Burton, K. Ong, T. Rea, I.Y. Chan: *Micropor. Mesopor. Mat.* **117** (2009) 75.
- [17] A.H. Morrish, P.E. Clark: *Phys. Rev. B* **11** (1975) 278.
- [18] H.St.C. O'Neill, A. Navrotsky: *American Mineralogist* **68** (1983) 181.
- [19] K.E. Sickafus, J.M. Wills, N.W. Grimes: *J. Am. Ceram. Soc.* **82** (1999) 3279.
- [20] R.D. Shannon: *Acta Cryst.* **A32** (1976) 751.
- [21] Database of Ionic Radii, Hosted by the Atomistic Simulation Group in the Materials Department of Imperial College, <http://abulafia.mt.ic.ac.uk/shannon/radius.php>
- [22] J.P. Chen, C.M. Sorensen, K.J. Klabunde, G.C. Hadjipanayis, E. Devlin, A. Kostikas: *Phys. Rev. B* **54** (1996) 9288.
- [23] D. Makovec, A. Kodre, I. Arcon, M. Drogenik: *J. Nanopart. Res.* **11** (2009) 1145.
- [24] L.K. Leung, B.J. Evans, A.H. Morrish: *Phys. Rev. B* **8** (1973) 29.
- [25] E.V. Gopalan, I.A. Al-Omari, K.A. Malini, P.A. Joy, D.S. Kumar, Y. Yoshida, M.R. Anantharaman: *J. Magn. Magn. Mater.* **321** (2009) 1092.
- [26] D. Carta, M.F. Casula, G. Mountjoy, A. Corrias: *Phys. Chem. Chem. Phys.* **10** (2008) 3108.
- [27] L. Cser, I. Dézsi, I. Gládkih, L. Keszthelyi, D.Kulgawczuk, N.A. Eissa, E. Sterk: *Phys. Stat. Sol.* **27** (1968) 131.

- [28] C. Rath, S. Anand, R.P. Das, K.K. Sahu, S.D. Kulkarni, S.K. Date, N.C. Mishra: *J. Appl. Phys.* **91** (2002) 2211.
- [29] C. Upadhyay, H.C. Verma, C. Rath, K.K. Sahu, S. Anand, R.P. Das, N.C. Mishra: *J. Alloys Compd.* **326** (2001) 94.
- [30] R. Mathur, D.R. Sharma, S.R. Vadera, S.R. Gupta, B.B. Sharma, N. Kumar: *Nanostruct. Mater.* **11** (1999) 677.
- [31] R. Gerber, G. Elbinger: *J. Phys. C: Solid State Phys.* **3** (1970) 1363.
- [32] R. Vautier, M. Paulus: *6.1.3.5.4 Curie temperatures.* in K.-H. Hellwege, A.M. Hellwege (eds.): SpringerMaterials - The Landolt-Börnstein Database. (DOI: 10.1007/10201438_65)
- [33] R. Massart, D. Zins, F. Gendron, M. Rivoire, R.V. Mehta, R.V. Upadhyay, P.S. Goyal, V.K. Aswal: *J. Magn. Magn. Mater.* **201** (1999) 73.
- [34] R.S. de Biasi, T.C. Devezas: *J. Appl. Phys.* **49** (1978) 2466.
- [35] Y.L. Raikher, V.I. Stepanov: *Phys. Rev. B* **50** (1994) 6250.
- [36] C. Kittel: *Phys. Rev.* **73** (1948) 155.
- [37] R.K. Wangsness: *Phys. Rev.* **93** (1954) 68.
- [38] S. Yoon, K.M. Krishnan: *J. Appl. Phys.* **109** (2011) 07B534.
- [39] S. Sakurai, S. Sasaki, M. Okube, H. Ohara, T. Toyoda: *Physica B* **403** (2008) 3589.
- [40] M. Wekesa, MD. Jamal Uddin, H.F. Sobhi: *Int. J. Chem. Res.* **2** (2011) 34.

Tables

Table 1. Lattice parameter (a), average crystallite size (d), inversion degree (i), anion parameter (u) obtained from X-ray diffractograms for $\text{Mn}_x\text{Zn}_{1-x}\text{Fe}_2\text{O}_4$.

x	a / nm	d / nm	i	u
0.05	0.84339(10)	4.9(1)	0.054(5)	0.38433(3)
0.1	0.84536(17)	6.2(1)	-0.004(7)	0.38495(5)
0.25	0.84363(14)	7.1(1)	0.133(6)	0.38441(4)
0.5	0.84327(12)	8.4(2)	0.258(5)	0.38430(4)
0.7	0.84218(11)	6.1(1)	0.390(5)	0.38396(3)
0.75	0.84113(12)	5.4(1)	0.454(5)	0.38363(4)
0.8	0.84289(35)	3.5(1)	0.405(14)	0.38418(11)
0.9	0.84528(71)	2.8(1)	0.353(28)	0.38492(22)

Table 2. The slope of the $B_{\text{SP},\parallel}(T)$ curve at $T \approx 140$ K ($\text{d}B_{\text{SP},\parallel}/\text{d}T$), effective anisotropy energy barrier ($E_a k_B^{-1}$), effective anisotropy energy density (K) and magnetic ordering temperature (T_c) determined on the basis of EPR spectra of $\text{Mn}_x\text{Zn}_{1-x}\text{Fe}_2\text{O}_4$.

x	$\text{d}B_{\text{SP},\parallel}/\text{d}T$ ($T = 140$ K) G/K	$E_a k_B^{-1}$ K	K KJ/m ³	T_c K
0.05	3.22(5)	99(9)	22.4(3.5)	440(5)
0.1	1.76(3)	31(6)	3.3(8)	301(5)
0.25	2.52(2)	48(6)	3.6(6)	360(5)
0.5	3.52(2)	152(9)	6.6(9)	470(5)
0.7	6.0(3)	108(17)	12.7(2.6)	500(5)
0.75	3.54(5)	183(13)	30(4)	720(24)
0.8	2.2(5)	34(22)	21(15)	508(10)
0.9	2.7(3)	63(20)	73(30)	529(5)

Figures

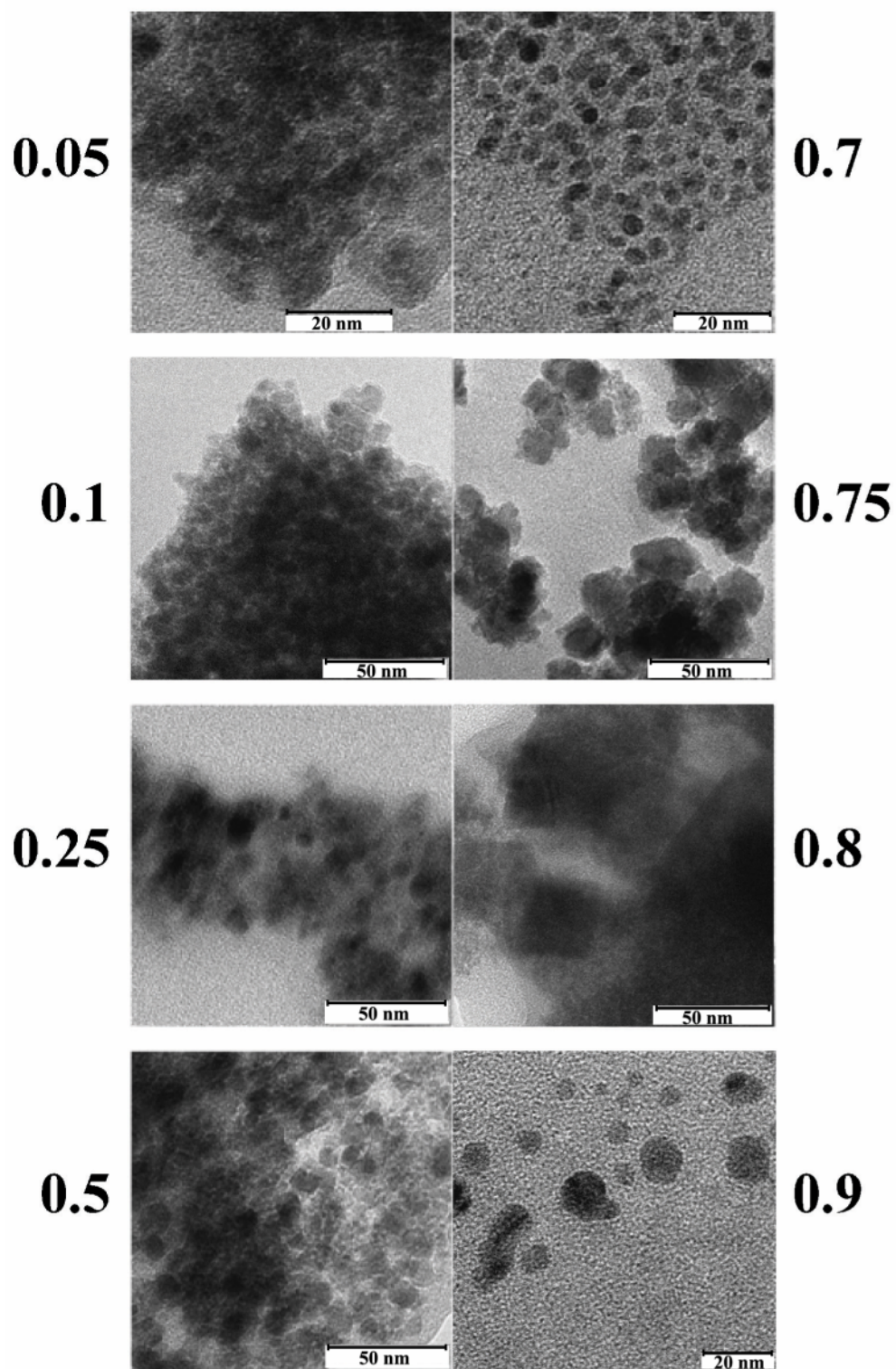


Figure 1. TEM images of the $\text{Mn}_x\text{Zn}_{1-x}\text{Fe}_2\text{O}_4$ spinel nanoparticles, with the x Mn concentration shown beside the corresponding image.

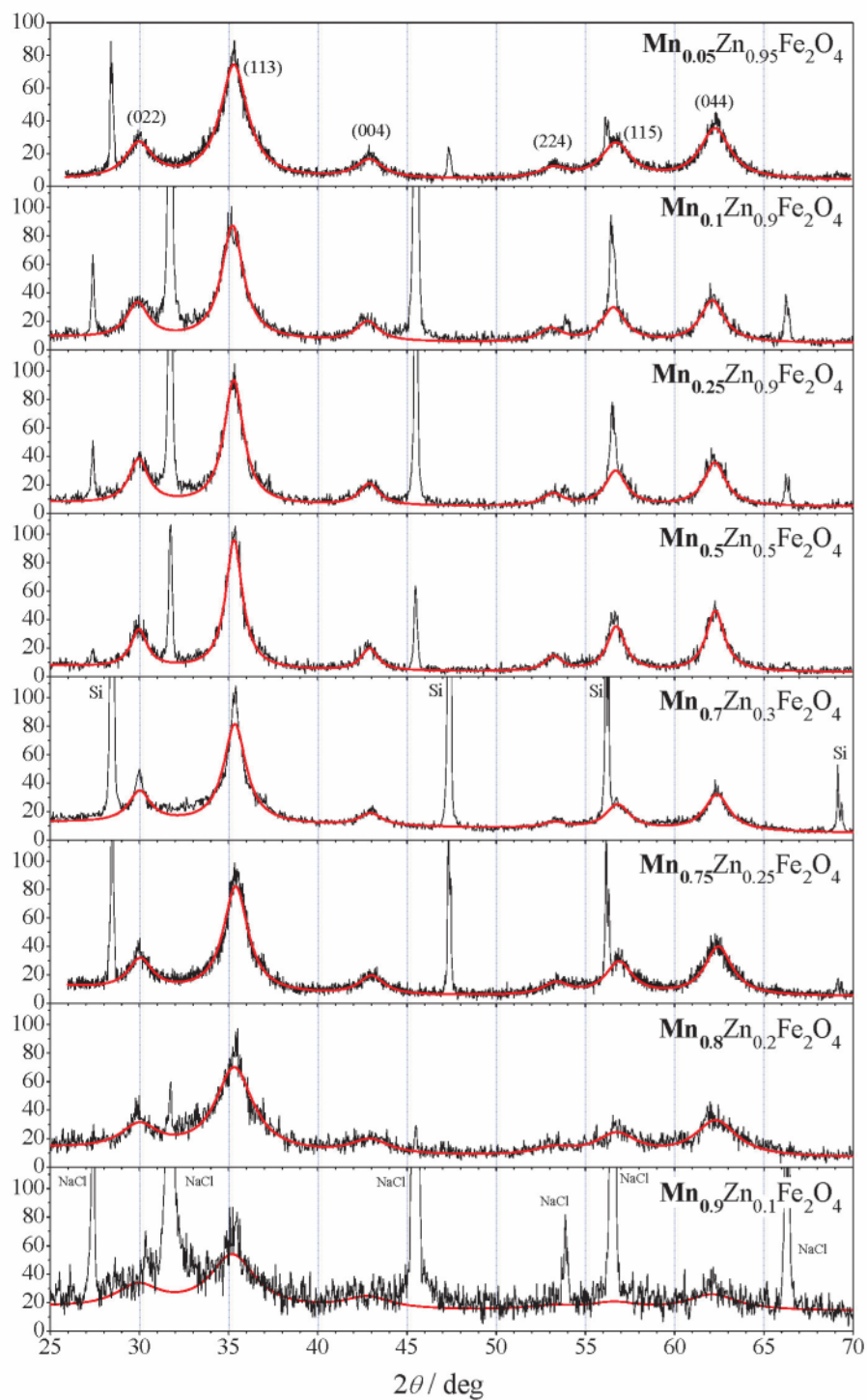


Figure 2. X-ray diffractograms of the studied $\text{Mn}_x\text{Zn}_{1-x}\text{Fe}_2\text{O}_4$ spinel nanopowders at room temperature, along with theoretical curves calculated for the cubic spinel phase.

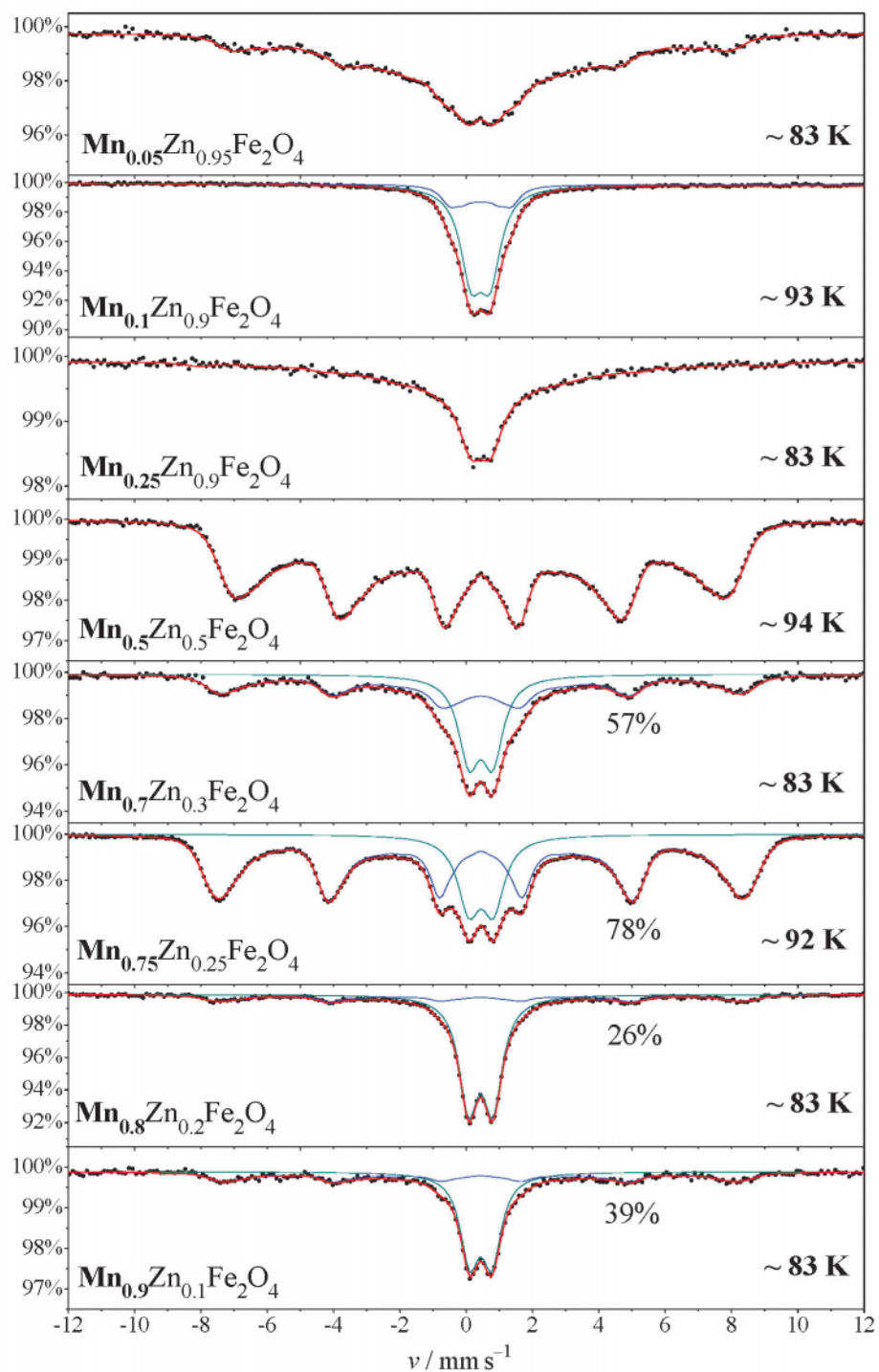


Figure 3. ^{57}Fe Mössbauer spectra of $\text{Mn}_x\text{Zn}_{1-x}\text{Fe}_2\text{O}_4$ spinel nanoparticles at the given temperatures. Percentage values (having a standard error of $\sim 1\%$) shown for $x = 0.7$ indicate the relative area fraction of the magnetic sextet component.

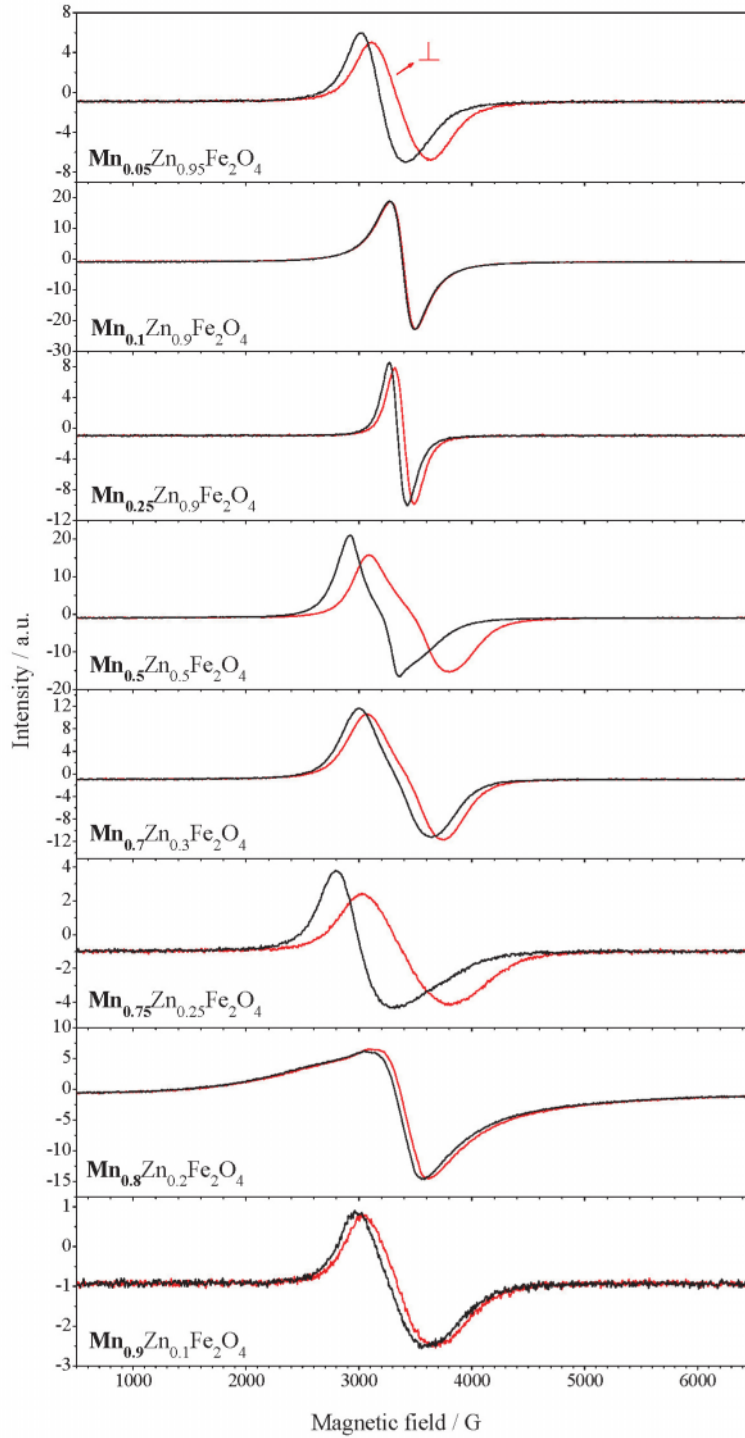


Figure 4. X-band EPR spectra of magnetically oriented $\text{Mn}_x\text{Zn}_{1-x}\text{Fe}_2\text{O}_4$ spinel nanoparticles at $T \approx 300$ K, with the direction of sample orientation being either parallel or perpendicular (\perp) to the scanning magnetic field.

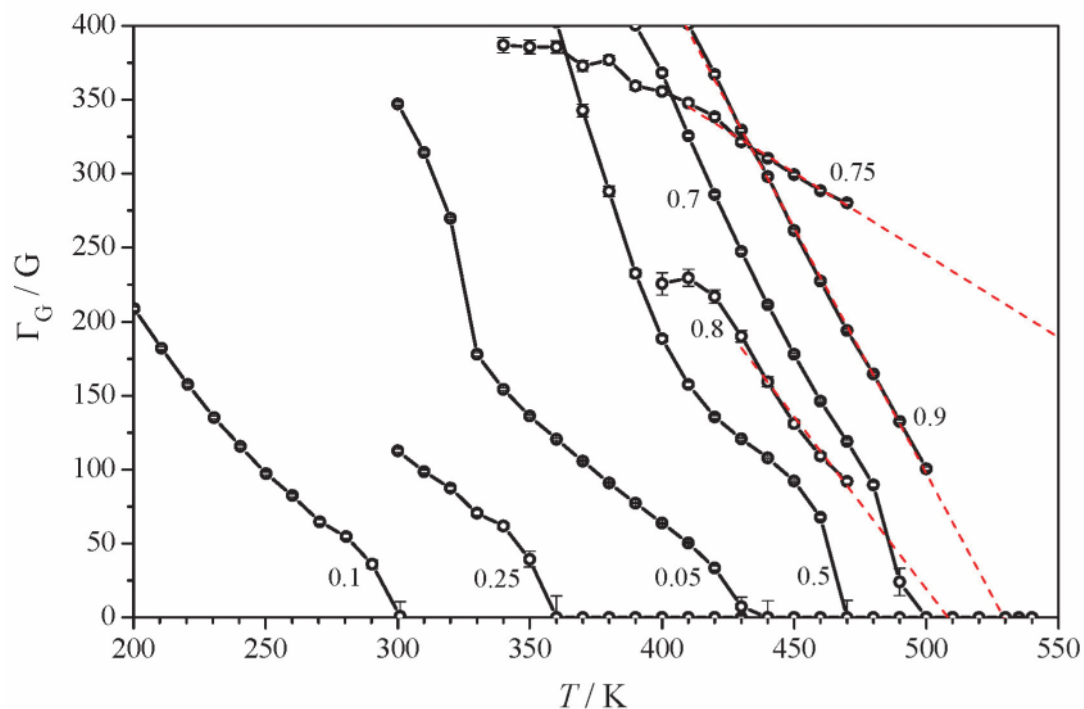


Figure 5. Temperature dependence of the Gaussian contribution (Γ_G , FWHM) to the width of EPR spectra of magnetically oriented $\text{Mn}_x\text{Zn}_{1-x}\text{Fe}_2\text{O}_4$ spinel nanoparticles.

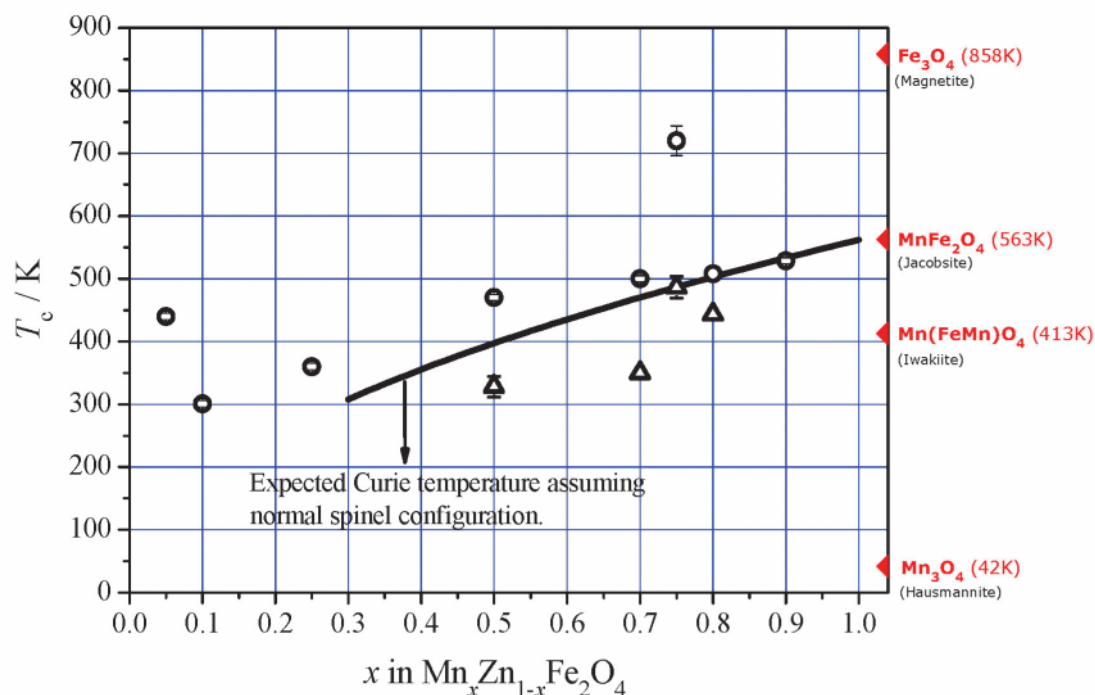


Figure 6. Curie temperatures estimated either on the basis of the temperature dependence of the Gaussian contribution to the FWHM width of the EPR spectra (Figure 5) (open circles), or on the basis of the temperature dependence of the hyperfine magnetic field values derived from the Mössbauer spectra (open triangles) for $\text{Mn}_x\text{Zn}_{1-x}\text{Fe}_2\text{O}_4$ nanoparticles. The curve drawn with a thick solid line corresponds to the expected variation of the Curie temperature in the case of normal (i.e. $i = 0$) $\text{Mn}_x\text{Zn}_{1-x}\text{Fe}_2\text{O}_4$ spinels [27,32]. The magnetic ordering temperatures of several spinel oxides are indicated on the right axis for the sake of comparison.

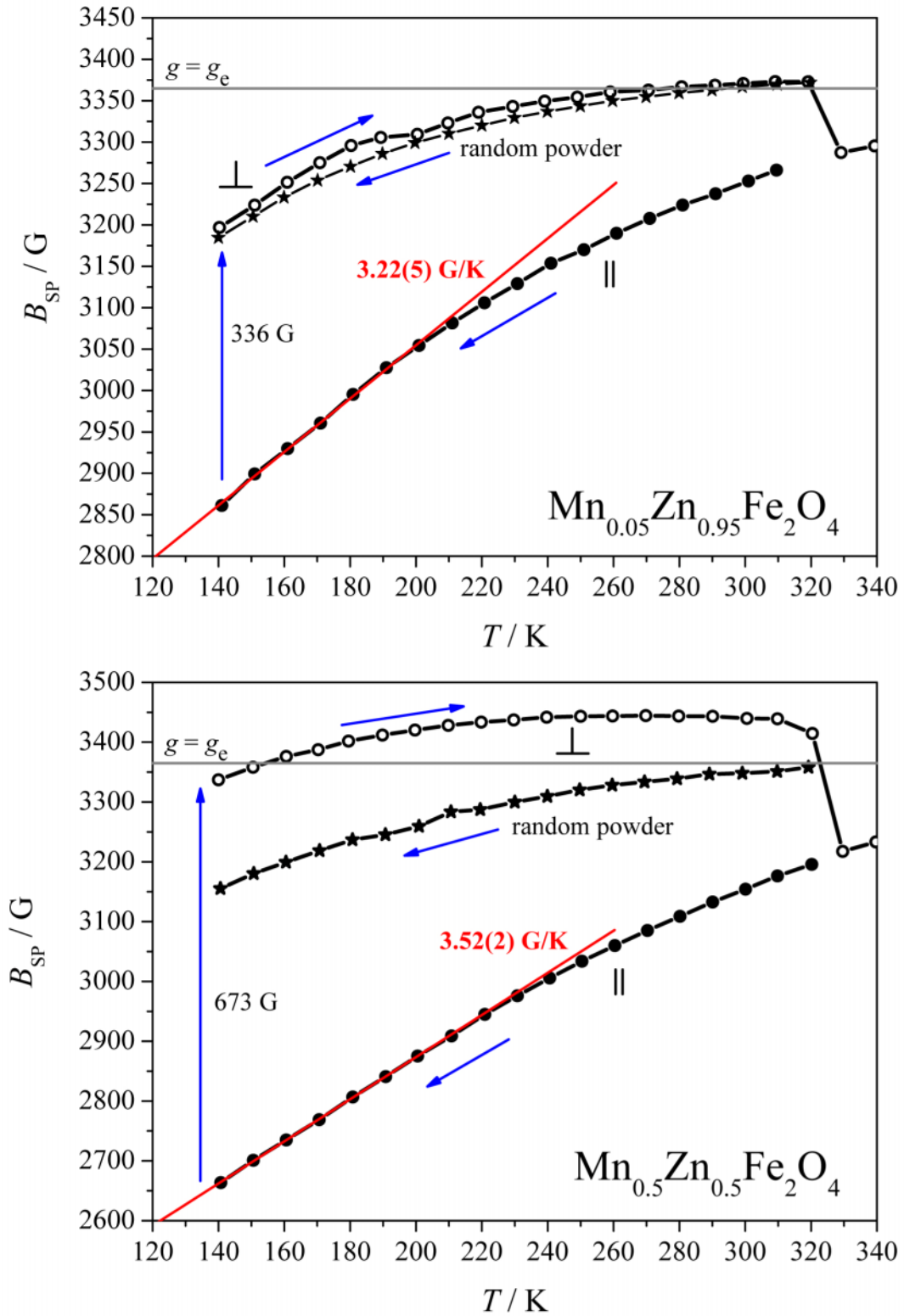


Figure 7. Typical examples of the temperature dependence of the central resonance field (B_{SP}) of the superparamagnetic peak detected in the EPR spectra of (1) wax-embedded oriented $Mn_xZn_{1-x}Fe_2O_4$ samples with the spectrometer's external sweeping magnetic field being either parallel (series of full circles marked by ||) or perpendicular (series of hollow circles marked by \perp) to the sample orientation, and of (2) MgO-mixed random $Mn_xZn_{1-x}Fe_2O_4$ powder (series of full stars).

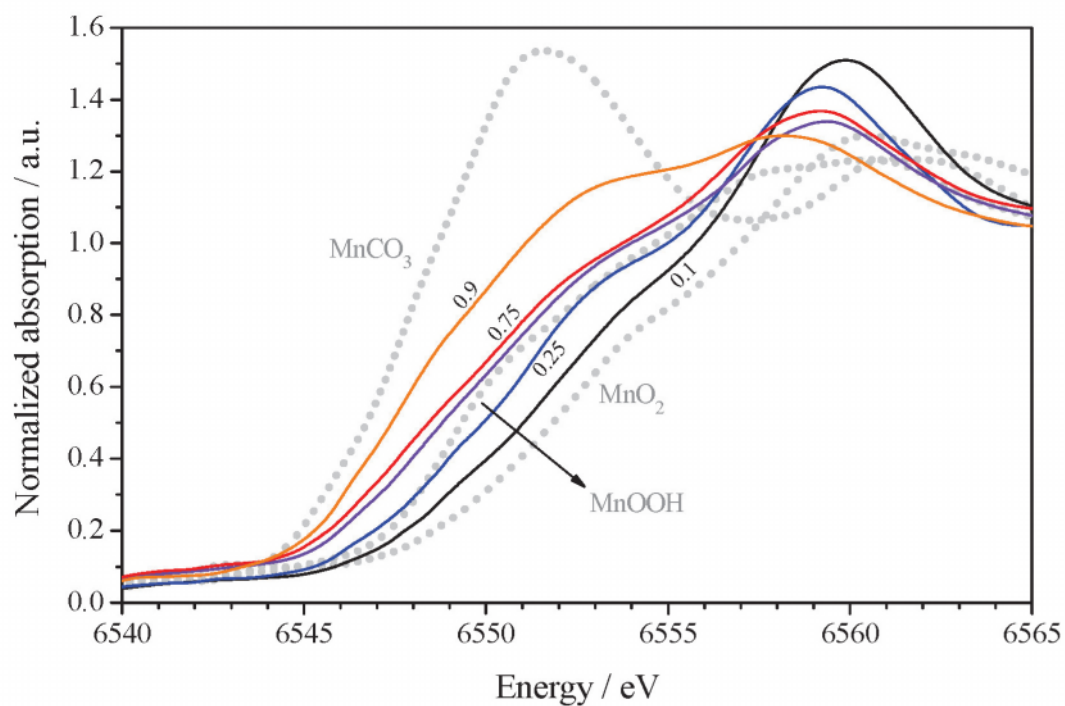


Figure 8. XANES spectra of the studied $\text{Mn}_x\text{Zn}_{1-x}\text{Fe}_2\text{O}_4$ nanoparticles with $x = 0.1, 0.25, 0.5, 0.75$ and 0.9 . The curve characterizing the sample with $x = 0.5$ is the one being closest – and slightly shifted to the right with respect – to the curve obtained for the sample with $x = 0.75$. Measurements of standards MnCO_3 , MnOOH and MnO_2 are shown as dotted lines.